Object Registration Techniques For 3D Particle Tracking

Hendriksen, L.A.; Sciacchitano, A.; Scarano, F.

DOI
10.55037/lxlaser.21st.113

Publication date
2024

Document Version
Final published version

Published in
Proceedings of the 21st International Symposium on the Application of Laser and Imaging Techniques to Fluid Mechanics

Object registration techniques for 3D particle tracking

L.A. Hendriksen[1,*], A. Sciacchitano[1], F. Scarano[1]

1: Dept. of Aerospace Engineering, Delft University of Technology, Netherlands
* Correspondent author: L.A.Hendriksen@tudelft.nl

Keywords: 3D-PIV, 3D-LPT, STB, HFSB, Object registration

ABSTRACT

Image based 3D particle tracking is currently the most widely used technique for volumetric velocity measurements. Inspecting the flow-field around an object is however, hampered by the latter, obstructing the view across it. In this study, the problem of measurement limitations due to the above is addressed. The present work builds upon the recent proposal from Wieneke and Rockstroh (2024), whereby the information of the occluded lines of sight can be incorporated into the particle tracking algorithm. The approach, however, necessitates of methods that accurately evaluate the shape and position of the object within the measurement domain. Methods of object marking and the following 3D registration of a digital object model (CAD) are discussed. For the latter, the Iterative Closest Point (ICP) registration algorithm is adopted. The accuracy of object registration is evaluated by means of experiments, where marking approaches that include physical and optically projected markers are discussed and compared. Three objects with growing level of geometrical complexity are considered: a cube, a truncated wing and a scaled model of a sport cyclist.

The registered CAD representations of the physical objects are included in aerodynamic experiments, and the flow field is measured by means of large-scale particle tracking using helium filled soap bubbles. Three operating regimes are studied and compared: monolithic, partitioned and object-aware (OA) monolithic. The results indicate that object registration enables a correct reconstruction of particle tracers and strongly reduces the domain clipping typical of the monolithic approach. Furthermore, the dynamical use of all views in the OA monolithic method offers clear benefits compared to the partitioned approach, namely a lower occurrence of ghost particles. Finally, the combined visualization of the object and the surrounding flow pattern offers means of insightful data inspection and interpretation, along with posing a basis for PIV data assimilation at the fluid-solid interface.

---

1. Introduction

Three-dimensional (3D) measurements of fluid flow velocity are currently performed with Particle Image Velocimetry (PIV) techniques that have evolved from the tomographic principle (Elsinga et al., 2006) towards individual particle tracking (Schröder & Schanz, 2023). Compared to tomographic PIV, particle tracking offers measurements with a higher dynamic range, lower data storage requirements and decreased computational time. Recent particle tracking experiments have reached measurement volumes of up to cubic meter scales (Jux et al., 2018; Schröder et al., 2022).

Upscaling of 3D experiments in air flows have been enabled with the introduction of helium filled soap bubbles (Bosbach et al., 2009) providing orders of magnitude higher light scattering compared to micron-sized droplets (Grille Guerra et al., 2024). The developments of 3D particle tracking have been further facilitated by advancements in system calibration (Wieneke, 2008), accurate particle image triangulation algorithms (Wieneke, 2013a) and the efficient and robust Lagrangian Particle Tracking algorithm *Shake-The-Box* (STB, Schanz et al., 2016). Despite the above advancements, most particle tracking experiments focus on simplified geometrical conditions such as boundary layers, free wakes or cavities (Schröder & Schanz, 2023). When an object is immersed in the flow, the measurement is hampered in the regions where the view or the illumination is blocked by the object. Hysa et al. (2023) have recently discussed the problem of estimating such volume losses when using a multi-camera 3D-PIV system, as a result of shadows and occlusion of camera views generated by one or more objects within the measurement volume. The erosion of the measurement volume caused by shadows is simply solved using two or more directions of illumination. In contrast, the problem of camera occlusion is of more complex nature as it entails the logics of 3D particle detection from a multitude of simultaneous views. The proposed practical solution has been that of partitioning the imaging system into multiple, independent subsystems (Hysa et al., 2023). Such approach showed benefits in terms of increased measurement coverage over the domain of interest, at the cost however, of a larger amount of ghost particles (Elsinga et al., 2011).

The recent work of Wieneke and Rockstroh (2024) proposes an algorithm that circumvents the requirement of a global (i.e. by all cameras) simultaneous view at every point of the measurement domain. The algorithm, however, requires the object position to be known a-priori, or experimentally determined, which opens up to the scope of the current work. Furthermore, the accurate determination of the object position within the measurement volume is beneficial for a number of reasons: it facilitates more accurate evaluation of near-surface flow properties such as pressure and skin friction (Depardon et al., 2005); it benefits data reduction, visualization and assimilation techniques through an accurate description of the fluid-solid interface (Cakir et al., 2022).

Approaches to 3D object position and orientation determination have been extensively studied in various domains, including medical imaging, machine vision and urban navigation for example (Saiti & Theoharis, 2020). The problem has been occasionally addressed in the PIV community. For instance Adhikari and Longmire (2012) proposed the *visual-hull* technique, whereby object silhouettes appearing within the camera images of a multi-camera setup are back-projected into physical space. Their intersection yields an approximate 3D hull, which encompasses the object within the measurement volume. This technique is applicable to moving objects and complex

shapes, making it a suited technique for flow measurements involving living animals as exemplified by Adhikari and Longmire, (2013), Mendelson and Techet, (2018) and Langley et al. (2014). The visual-hull technique, however, suffers from the inability to detect concave regions and relies on edge-detection, with specific requirements on the object appearance- and illumination conditions, which often conflict with the need to detect the light scattered by the tracer particles in front of the object.

In Jux et al. (2021), an in-situ approach to object surface reconstruction solely based on flow tracers is introduced, where the void in particle distributions is associated with the presence of a solid object. The method reconstructs satisfactorily simple, smooth objects but it requires a high particle concentration to reconstruct complex shapes or to deal with sharp edges.

In aircraft aerodynamics, studies dealing with object motion and deformation have made use of surface markers (Liu et al., 2012) with most frequent focus on structural deflection monitoring and not on the evaluation of fluid motion. Markers, either printed or projected onto the surface are among the most practiced methods (Pappa et al., 2003). The use of a speckle pattern enables a dense and more accurate determination of object position and deformation, according to the Digital Image Correlation method (Pan, 2018). More recently, the DIC technique has been combined with image-based volumetric flow measurements in the context of Fluid Structure Interaction (FSI) in Acher et al. (2019) and Zhang et al. (2019) who adopted separate measurement systems to determine simultaneously the structural behaviour of an aerodynamic test object and the flow around it. Measuring both structure and fluid using a single measurement setup has been demonstrated by e.g. Jeon and Sung. (2012) when the surface markers can be separated from the flow markers.

Many advancements have been obtained within the European HOMER (Holistic Optical Metrology for Aero-Elastic Research) project. The work by Mitrotta et al. (2022) uses the shake-the-box (STB, Schanz et al. 2016) algorithm for simultaneous measurements of retro-reflective surface markers and helium filled soap bubbles for the air motion. Mertens et al. (2023) applied a similar approach to estimate structural-, inertial- and aerodynamic forces on a flexible wing solely from optical measurements. Obtaining an estimate of a continuously deforming elastic object from discrete points was achieved using polynomial functions that fit across the positions of few markers printed on the surface. The method was demonstrated to reconstruct the motion of a thin, flexible sheet subject to the Kármán wake past a circular cylinder (Saiz et al., 2022). In some cases, direct tessellation of measured markers can be adopted, provided that their spatial density suffices (Jeon & Sung., 2012).

The current work examines the process of object registration in 3D-PIV experiments, where a single set of cameras are used to render simultaneously the 3D velocity field along with the object

position, with the aim of enhancing and simplifying the use of multi-camera systems for 3D aerodynamic experiments around complex objects. The study discusses first the problem of object registration, based upon the principles of the Iterative Closest Point (ICP) algorithm (Besl and McKay, 1992). Different approaches to object marking are examined and compared by means of laboratory experiments in terms of model surface coverage, registration accuracy and practicality. Furthermore, the feasibility of object registration for accurate particle reconstruction and data interpretability (in presence of object induced camera occlusion) for 3D-PIV are illustrated presenting three flow experiments that involve models of increasing geometrical complexity.

2. Iterative Closest Point algorithm

The alignment of a 3D CAD model with the measured views of the corresponding object placed in the physical space and observed from several views is known as 3D object registration. Such task is frequently encountered in the field of computer vision (Saiti & Theoharis, 2020). In 3D-PIV systems, object registration becomes necessary to identify regions of shadow and (partial) camera occlusion, which affect particle illumination and reconstruction. When the geometry of the object is known a-priori (e.g. most commonly as a CAD model used for manufacturing) the registration problem translates into the search for a transformation (translation and rotation) that brings the CAD model to accurately overlap with the object placed in physical space. Object registration comprises three steps: 1) the position of the CAD model is initialised (initial guess); 2) The disparity between model position and the actual object is estimated through an error metric; 3) A transformation is found such that the aforementioned error metric is minimized. An example of a CAD model (grey-shaded geometry) before and after being registered to a set of points (red dots) is shown in figure 1.

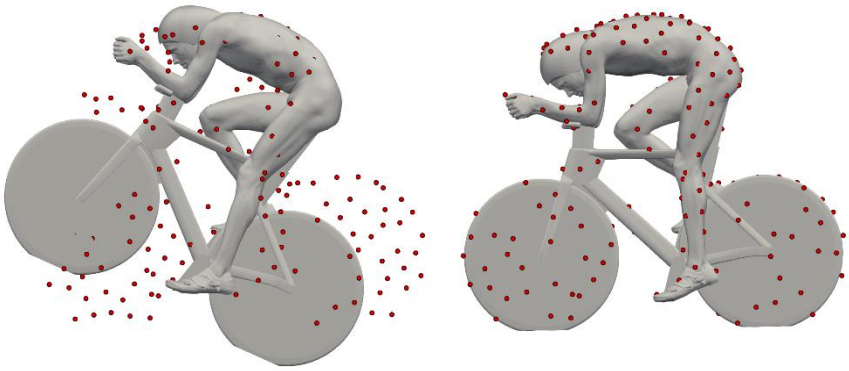

Figure. 1 Illustration of the initial and final position of the cyclist CAD model registration based on experimental pointwise surface measurements of the marked object (red points).

A commonly used registration algorithm is the Iterative Closest Point (ICP, Besl and McKay 1992), because of its relative simplicity and efficient implementations in open source programming libraries (Zhou et al., 2018). The working principle of two variants of this algorithm for CAD model registration are illustrated in figure 2.

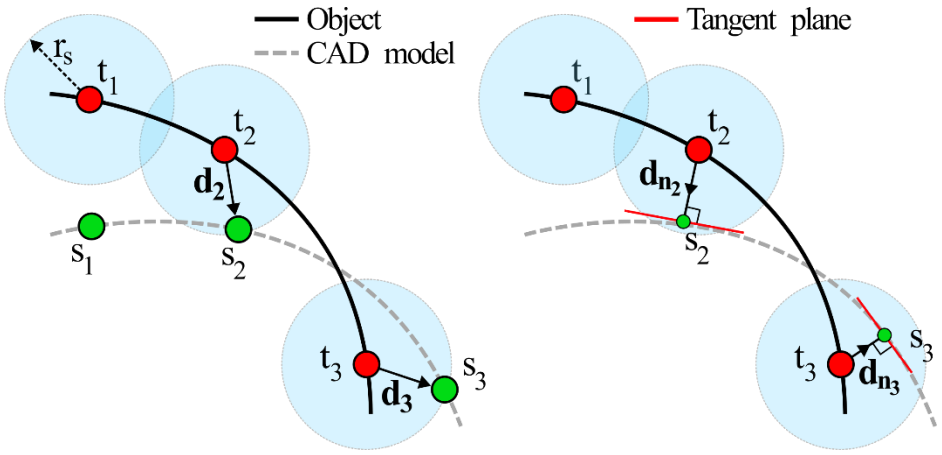

Figure. 2 Schematics of the working principle for point-to-point ICP (left) and point-to-plane ICP (right) for the registration of arbitrarily shaped CAD models to experimental object surface measurements. Registration based on the minimization of an error metric defined between the target points (red, object) and source points (green, CAD model).

The ICP algorithm making use of a point-to-point error metric (figure 2, left) relies upon the assumption that the object is marked at prescribed locations on its surface (see section 3.1 for object marking techniques), for instance during manufacturing. The markers' coordinates are collected as the target point cloud $\boldsymbol{t}$. Correspondingly, the CAD model includes a set of points (virtual markers) referred to as the source point cloud $\boldsymbol{s}$. Starting from an initial guess, the ICP algorithm iterates over three steps: selection, matching and minimization (Rusinkiewicz & Levoy, 2001). In the selection step, a search radius r_s is defined which determines the maximum distance a target point in $\boldsymbol{t}$ is allowed to search for a source point in $\boldsymbol{s}$. Large search radii improve the chance of matching, but make the process more prone to finding erroneous alignments. A (too) small search radius instead, improves unicity of the registration, at the risk however, of "short sightedness" of the algorithm, whereby many valid points may be discarded (Segal et al., 2009). In the matching step, target points are corresponded with their closest source point within the search radius. The established set of corresponding pairs is referred to as the correspondence set $\boldsymbol{K}$. A rigid body transformation matrix $\boldsymbol{M}$ is found, under which the following error metric $\epsilon(\boldsymbol{M})$ is minimized.

$$\epsilon(\boldsymbol{M}) = \sum_{(s,t\,\in K)} \left|\left|\boldsymbol{M}\boldsymbol{s} - \boldsymbol{t}\right|\right|^2 \tag{1}$$

The three steps are repeated until convergence. Since this involves direct minimization over the distance between corresponding point pairs, it is referred to as point-to-point ICP. In many applications however, as introduced in section 3.2, the application of surface markers at prescribed locations on an object is not practical. In these circumstances the so-called point-to-plane ICP variant (Chen & Medioni, 1992) is more generally applicable (Pomerleau et al., 2013). Point-to-

plane ICP follows the same three steps, with some slight differences explained below and represented in figure 2-right.

Identical to point-to-point ICP, the registration is initialised from an initial guess of the CAD model position with respect to the estimated object position. A search radius is defined which allows the target points to find parts of the CAD model that lie within this distance. For each target point, the closest point on the CAD model surface (within the search radius) is computed and referred to as a source point. These source and target points form the correspondence set $\boldsymbol{K}$. Instead of using direct point-to-point distances for error metric minimization, the rigid transformation $\boldsymbol{M}$ aims at minimizing the distance $\boldsymbol{d_n}$ between the target points and the local tangent planes of the source points (see equation 2). Hence the name point-to-plane ICP.

$$\epsilon(\boldsymbol{M}) = \sum_{(s,t\,\in K)}\left((\boldsymbol{Ms} - \boldsymbol{t}) \cdot \boldsymbol{d_n}\right)^2 \tag{2}$$

Note that different from point-to-point ICP, the point-to-plane ICP requires computation of the source points s at each iteration. Source points are therefore not fixed with respect to the CAD model. They rather float on its surface, depending upon the presence of target points within the search radius. Unless the distribution of the source points is known, the point-to-plane ICP is adopted in the present work.

3. Experimental setup and measurement procedures

3.1 Test objects

Different test objects with increasing geometrical complexity are used in the present study: a cube of 12 cm side-length, a truncated wing of 18 cm chord length (and 10.8 cm span) and a 1:8 scaled cyclist of 22 cm length (wheeltip to wheeltip).

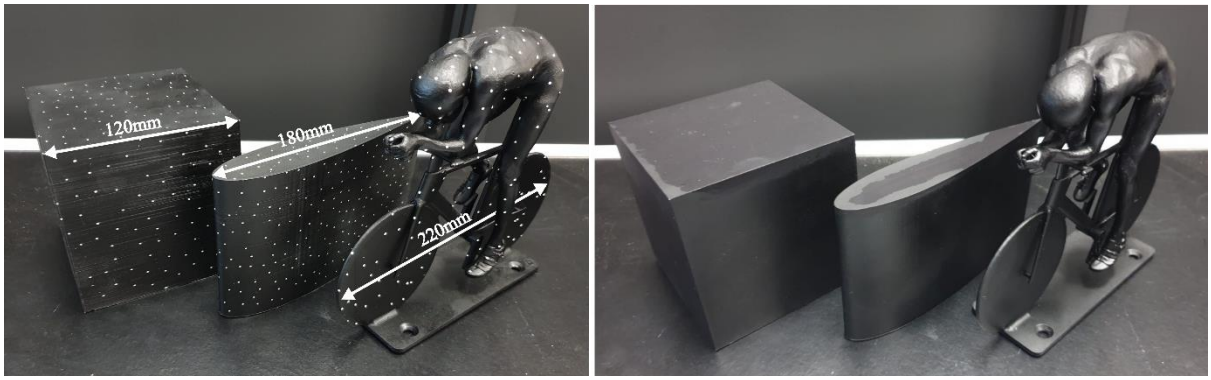

Figure. 3 Manufactured cube, truncated wing and scaled cyclist test objects. Version including incorporated retro-reflective markers on the left and version left plain mat black on the right.

The cube and wing are 3D printed using Fused Deposition Modeling (FDM) and the cyclist with stereolithography. The nominal manufacturing accuracy of the cube, wing and cyclist are approximately 0.3 mm, 0.1 mm and 0.1 mm respectively. Two versions of each object are produced; one includes retro-reflective markers of 1.2 $mm \pm 0.1\ mm$ diameter, positioned at known locations, which enable the use of the point-to-point ICP registration technique (section 4.1). The other is

marker free (plain mat black) and are used to investigate active optical marking as discussed in section 3.3. The manufactured objects are shown in figure 3.

3.2 Imaging system

The imaging system comprises seven CMOS cameras (1Mpx, 5,400 fps) subtending a wide solid angle above and around the object (see figure 7). Two directions of illumination are provided by two LaVision flashlight-300 LED's. The total measurement volume is approximately $40 \times 40 \times 30\ cm^3$, which includes the whole model and some of the ground plate around it. A summary of the parameters for the imaging setup and particle tracking are provided in table 1 and table 2.

Table. 1 Imaging system and parameters.

Camera		C1	C2	C3	C4	C5	C6	C7
Resolution	[px]	1024 x 1024						
Pixel pitch	[µm]	20						
Focal length	[mm]	60	50	60	50	60	50	60
F-number		32	22	22	16	22	22	32
Magnification		0.05						
Angular camera offset	[°]	45						

3.3 Object marking and measurements

Three surface marking techniques are employed: 1) markers are incorporated at prescribed locations during the manufacturing process; 2) the object is illuminated at a single point with a beam laser pointer; 3) the laser beam is split into a multitude of directions resulting in simultaneous multi-point optical marking (approximately 10 to 20 points on the object surface).

The first technique requires object illumination, which is provided by the LED system (figure 4-a). As such, the images require pre-processing to eliminate the light reflected from the model surface, by means of sliding minimum subtraction and intensity normalization. Despite a single image being sufficient for the triangulation of the surface markers in theory, a set of 100 recordings is collected to reduce the background noise (sequence minimum intensity subtraction). Any residual low intensity background is removed by subtracting a constant, low-value intensity. An example of a pre-processed image of the cyclist including incorporated markers and illuminated with LED is shown in figure 4-b. The resulting images return easily detectable surface markers with the iterative particle reconstruction algorithm (IPR, Wieneke, 2013), available in the LaVision DaVis 11 software.

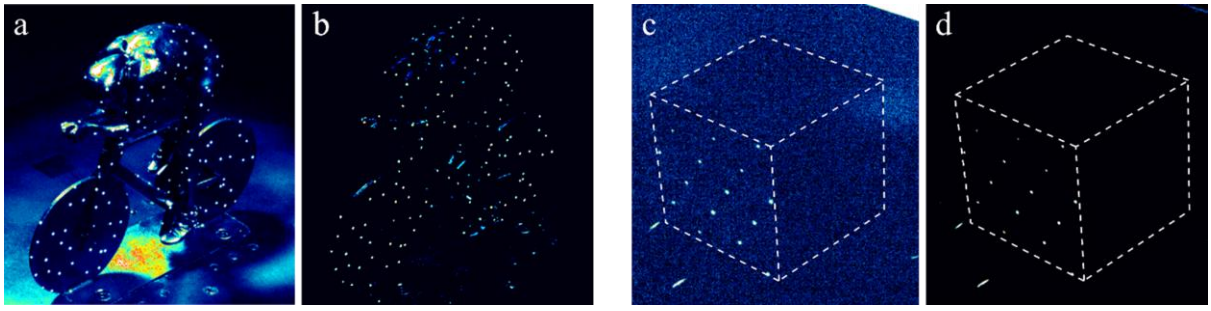

Figure. 4 Raw (a) and pre-processed (b) image of the cyclist object with incorporated markers illuminated with LED light. Raw (c) and pre-processed (d) images of the cube (in dark environment) marked with multi-point laser.

While illuminating the objects with the laser pointer, LED illumination is not needed, which leads to images with minimal background intensity from ambient light. Images of the objects are acquired at a frequency of 25 Hz while manually sweeping the laser pattern across the object surface, which is sufficiently covered in under a minute (approximately 1000 images are recorded). A single image of the cube, illuminated with the multi-point laser is shown in figure 4-c and the pre-processed result in figure 4-d. In this case, the 3D positions of the marked points are triangulated, using IPR, at each frame separately and later combined to provide a dense cloud of target points. Examples of the target point clouds obtained using three different object marking techniques on the cyclist are shown in figure 5. Incorporated markers appear with the lowest surface concentration as they are constantly present during the experiment and interfere with the process of flow tracer detection when their images overlap. Laser marking is performed prior to the experiment and an arbitrarily large number of points can be accumulated. The multi-point marking technique allows increasing further the number of marked points, as shown in figure 5-c.

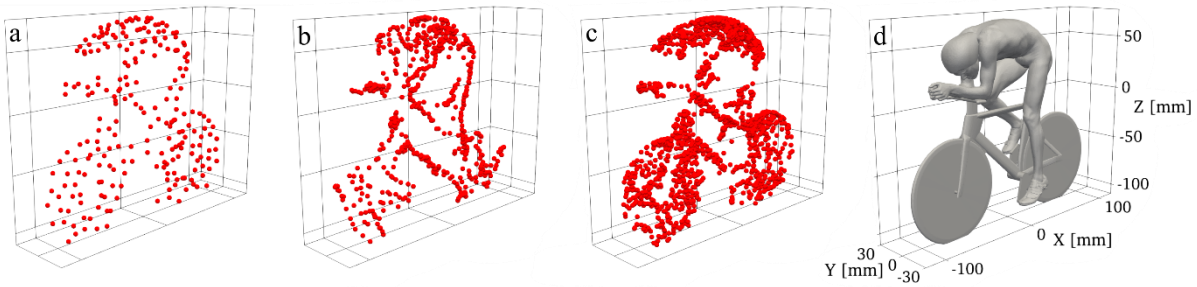

Figure. 5 Target point clouds as obtained from different object marking techniques on the cyclist. a) Incorporated markers. b) Single-point laser markers. c) Multi-point laser markers. d) Cyclist CAD model as reference.

3.3.1 Optical coverage of the marked objects

Not all sides of the object can be viewed from all directions. For the same principle, also the markers cannot be viewed simultaneously by all cameras. Following the discussion in Hysa et al. (2023), the detection rule that a marker is recognized only if present in all views will be referred to as monolithic, in that the imaging system operates in the whole measurement domain as a single entity. In this case the marker detection process is hindered at several parts of the object surface, leading to measurement volume erosion. figure 6-a, illustrates the condition where all seven cameras are used in a monolithic configuration to triangulate the markers produced by projecting a multi-point laser onto the cube's surface. Only the top face of the cube is in view to all cameras simultaneously. As a result, only those markers are detected, while those on the sides cannot be measured as they are partly obscured to some cameras. Paradoxically, increasing the number of cameras in a monolithic imaging system further erodes the measurement volume. To overcome this problem in a multi-camera setup, the imaging system can be partitioned into a number of independent groups (Hysa et al., 2023). In figure 6-b, groups of three cameras are considered to detect the same markers. An increase in the surface area onto which markers can be triangulated is apparent, strongly benefiting the object registration. Partitioning further into more groups of only two cameras maximizes the amount of object surface where markers can be detected, as shown in figure 6-c. An inverse relationship exists, however, between the number of cameras involved in 3D triangulation and the formation of false triangulations (ghost particles, Elsinga et al., 2011), which complicates the process of object registration.

Considering the above, marking the object using only a single point at a time (e.g. from a laser pointer), eliminates the problem of ghost particle formation even when only two cameras are used for the triangulation. This is illustrated in figure 6-d. To avoid excessive ghost particle formation while maximizing surface coverage, both incorporated markers and multi-point laser markers are triangulated using a partitioned setup with a group size of three cameras. For the triangulation of the single-point laser markers, group sizes of two are used instead.

Note that the problem of measurement volume erosion in a monolithic setup also holds for the 3D triangulation of flow tracers around 3D objects as will be discussed in section 4.3 and 4.4. A partitioned approach with small groups (2 to 3) of cameras, such as that used in Hysa et al. (2023) to increase the volume coverage comes, however at the cost of a higher occurrence of ghost particles. It may therefore only be viable for the object registration and not for flow marker tracking in which the particle density is typically considerably higher.

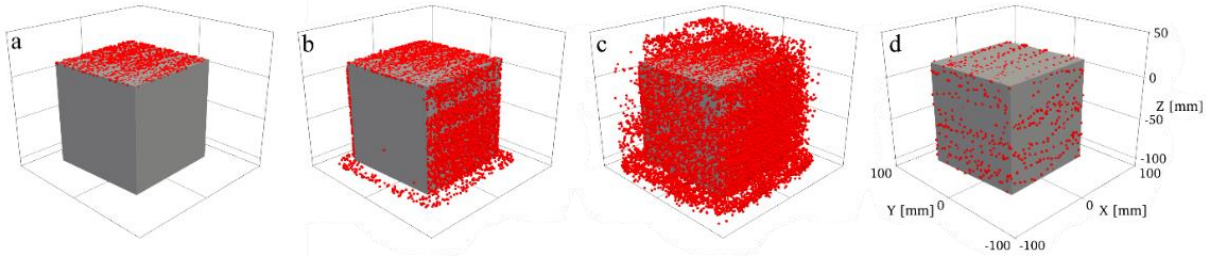

Figure. 6 Markers detected on the surface of the cube object as produced from multi-point laser projection. a) Monolithic approach, b) partitioned approach with groups of three cameras and c) two cameras. d) Detected markers as produced from single point projection with the partitioned approach with groups of two cameras.

3.4 Wind tunnel measurement conditions

Volumetric flow measurements are performed through large-scale particle tracking. The experiments are performed in a low-speed open jet wind-tunnel, featuring a $60 \times 60\ cm^2$ cross-section, where a flat plate with elliptical leading edge hosts the selected object. The free stream velocity is $8\ m/s$ or $10\ m/s$, depending on the object, with approximately 1% turbulence intensity. A schematic is provided in figure 7.

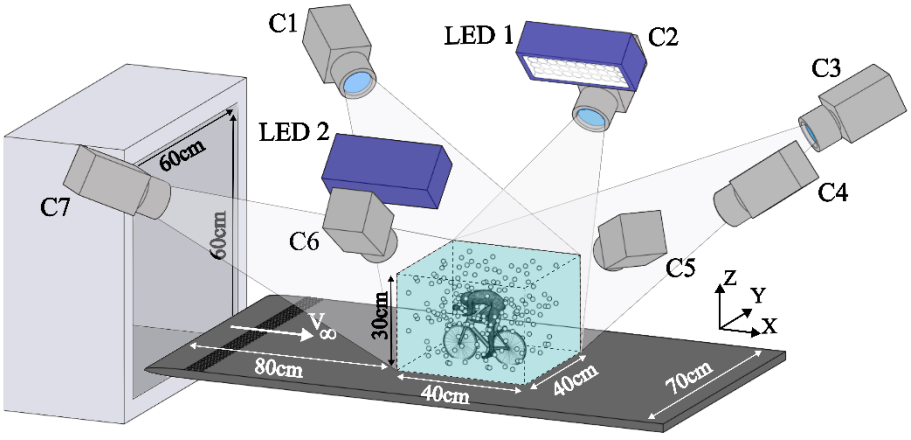

Figure. 7 Experimental setup for both velocity field and object registration measurements: seven camera imaging system, LED-illumination, HFSB flow tracers and a plate for model mounting positioned downstream of an open-jet wind-tunnel.

The flow is seeded with Helium Filled Soap Bubbles (HFSB, Bosbach et al., 2009) by a $0.5\,m \times 1\,m$ seeding rake containing 200 bubble generators upstream of the wind-tunnel contraction. The mean diameter of the neutrally buoyant bubbles is $350\,\mu m$ and at a production rate of $6 \times 10^6\ bubbles/s$ (Saiz et al., 2022) a seeding concentration of 1.2 bubbles per cubic centimeter (b/cm^3) is achieved at $10\ m/s$ freestream velocity. The seeding density in the images is approximately 0.02 particles per pixel (ppp). The pre-processed images are used as input for the Shake-The-Box particle tracking algorithm available in DaVis 11. The measurement conditions are summarised in table 2.

Table. 2 Wind tunnel experiment parameters.

Freestream velocity	[m/s]	8 (cyclist) 10 (wing, cube)
Measurement volume	[cm^3]	$40 \times 40 \times 30$
Seeding concentration	[b/cm^3]	1.2
Acquisition frequency	[Hz]	3000
Images per run		5000
Particle image density	[ppp]	0.02

Velocity measurements are performed around each of the objects by tracking the HFSB inserted in the flow in the wind tunnel settling chamber. The freestream velocity for the cyclist case is $8\ m/s$ and for the cube and wing it is $10\ m/s$. This yields Reynolds numbers of 60,000, 80,000 and 120,000 respectively (cyclist torso length $= 90\,mm$ is used as reference length). Images are recorded at a rate of $3kHz$. For each object, a measurement consists of 5,000 images for a duration of $1.67\,s$. The same conditions are repeated with the objects that incorporate retro-reflective markers. A raw instantaneous image of the cyclist model immersed in the flow is shown in figure 8-left.

For a reliable particle detection, background reflections need to be removed. The image pre-processing operations involve minimum pixel intensity subtraction and image intensity normalization. Finally, a small constant value ($2-3\%$ of particle peak intensity) is subtracted to eliminate residual low intensity noise in the background. The effectiveness of the pre-processing steps is shown in figure 8-right.

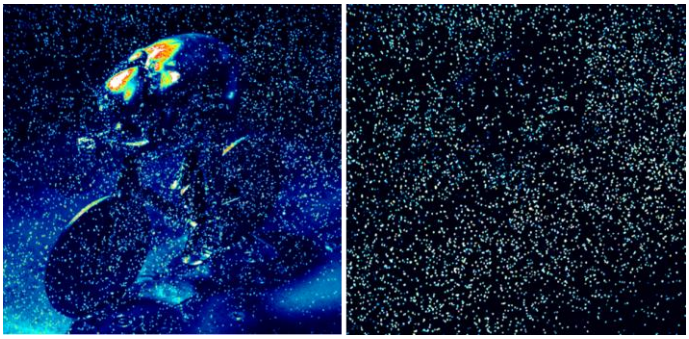

Figure. 8 Raw (left) and pre-processed (right) recording of the plain black scaled cyclist object immersed in HFSB seeded flow.

4 Results

4.1 Point-to-point registration

In this section, the accuracy of the object registration process is evaluated by comparing the results with a reference registration obtained for each of the objects. Such reference registrations are performed making use of the objects that include incorporated markers at known positions. Therefore, the point-to-point correspondence is imposed, which is considered the most accurate and robust option. Yet, imperfection in marker triangulation and in the manufacturing of the test objects result in a finite residual after the reference registration.

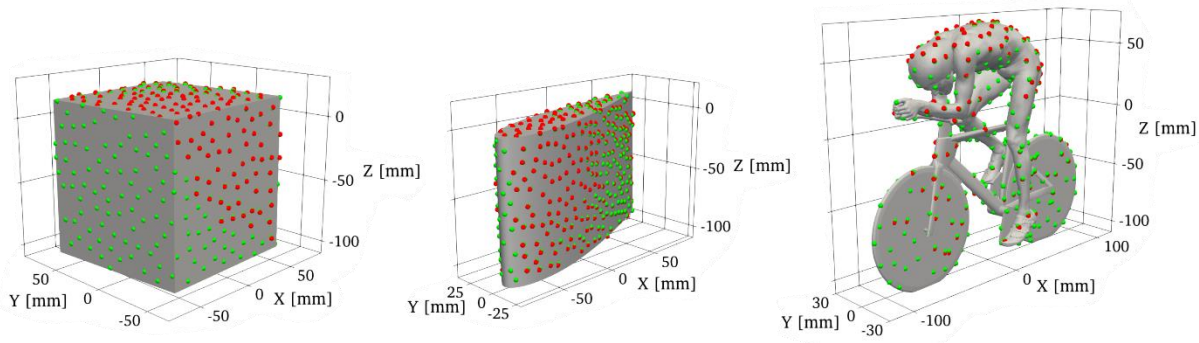

Figure. 9 Reference (point-to-point) registrations for the three objects. Green dots represent the distribution of the incorporated markers on the object surface (source ***s***). Red dots represent the experimentally triangulated and registered markers (target ***t***).

The incorporated markers are detected and triangulated following the procedure described in section 3.3, resulting in a set of target points t for each object. The corresponding CAD model is virtually marked providing the source points s. In this scenario a direct correspondence exists between the target and source points and point-to-point ICP can be applied. The result of the registration is shown in figure 9, where the red dots indicate the triangulated position of the incorporated markers on the object surface (target, t). The green markers, instead, are the source points s associated to the CAD representation of the model. As it can be observed in figure 9 a subset of the source points is matched to the triangulated target points. Reasons for unmatched source points are twofold: first, some target points are simply not triangulated as they are not in view by the set minimum number of three cameras (see section 3.4). Second, correspondences between source and target points in the ICP registration procedure are established based on the defined search radius as mentioned in section 2. Target points without a corresponding source point within the search radius ($r_s = 1.5\,mm$ is used) are not visualized as they are ignored during the registration procedure. Statistics in terms of distance from target to source points are provided in the histograms below.

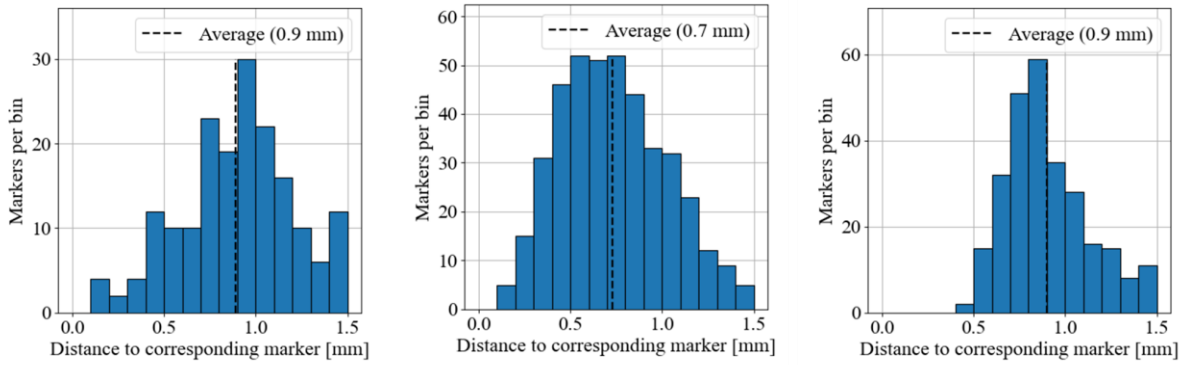

Figure. 10 Histograms of distance between marker correspondences after reference object registrations. Left to right for the cube, truncated wing and scaled cyclist respectively.

For the cube, wing and cyclist, 66%, 92% and 46% respectively, of the surface markers are triangulated and matched within 1.5 mm. The average discrepancy (distance between the triangulated target point and the corresponding source point position) is 0.8 mm. Such discrepancy is associated to the 3D triangulation uncertainty as well as that of model manufacturing. It is observed that triangulation of the incorporated markers is consistently offset from the true marker location by a distance in the order of the marker radius. Furthermore, large markers, in combination with the direction of illumination are an additional source of uncertainty in the determination of the marker centers.

4.2 Point-to-plane based object registrations

The reference registrations are used as a baseline to assess the registrations based on the different marking techniques. A comparative analysis is made of three methods: incorporated markers (without making use of their known distribution as done for the reference registration), projection of a single laser point, or multitude of points along the object surface. Furthermore, these techniques are applied to three objects, resulting in nine conditions for the object registration. figure 11 illustrates three registration examples each on a different object, where target points are color-coded with the distance to the registered CAD model surface. These object registrations make use of point-to-plane ICP. The object registrations are performed using a final search radius of 1.5 mm; hence, only those markers within a distance to CAD model surface below 1.5 mm are included in the figures.

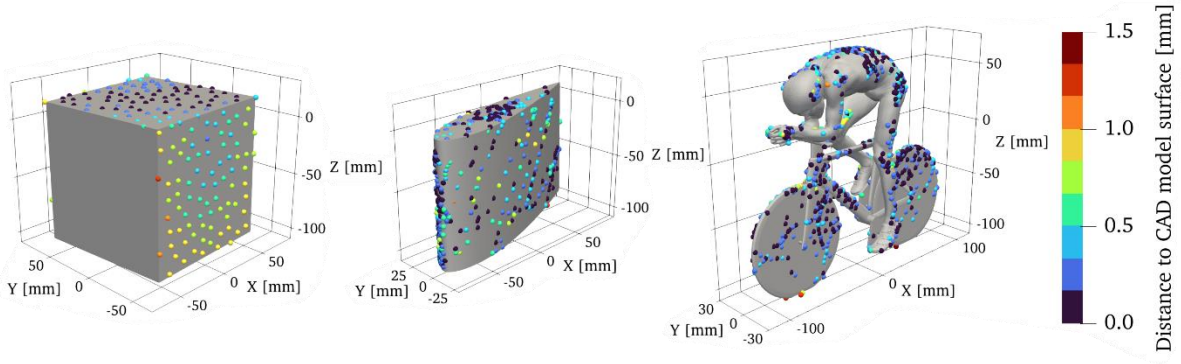

Figure. 11 Example object registrations of the cube with respect to triangulated incorporated markers (left), truncated wing to single-point laser markers (middle) and scaled cyclist to multi-point laser markers (right).

For the incorporated markers on the cube, a partitioned system, where cameras are arranged in triplets is used (see section 3.3.1). Since the front face of the cube is in view by only two cameras, markers on the frontal face are not reconstructed. On the side face of the cube, the discrepancy varies within $0.5 - 1.0\,mm$, with a pattern indicating a non-flat cube face. The top face yields consistently smaller errors. Yet, some gradient towards the cube corners indicates some degree of warping due to thermal effects during the 3D printing. The truncated wing and cyclist yield lower values of the discrepancy with no specific spatial pattern, indicating a smaller effect of manufacturing artefacts in these cases. The mean values of markers discrepancy, denoted $\delta_{s,t}$ (discrepancy between source s and target t), are reported in table 3.

Table. 3 Object registration results in mean absolute distance from markers to registered CAD model ($\delta_{s,t}$).

$\delta_{s,t}$ [mm]	Cube	Wing	Cyclist
Incorporated markers	0.473	0.274	0.278
Multi-point laser	0.482	0.186	0.258
Single-point laser	0.513	0.275	0.352

The cube registration yields a $\delta_{s,t}$ of about 0.5 mm, with only minor differences among the marking techniques. For the truncated wing and scaled cyclist, $\delta_{s,t}$ is around 0.3 mm and variations among marking techniques below 0.1 mm. The registration performed using the single-point laser marking yields the largest values of $\delta_{s,t}$. This is not ascribed to the limited number of points, but rather a side effect of the increased surface coverage achieved using the partitioned approach with camera pairs instead of triplets (see section 3.3.1). The increased coverage imposes a stricter constraint to the model registration as the point-to-plane algorithm allows some relative sliding. Increased model surface coverage with a given marking technique is expected to benefit the determination of the model position through registration; however, this is not necessarily represented in the average distance from markers to the CAD model $\delta_{s,t}$. Therefore, the Dice Similarity Coefficient (DSC, Dice, 1945) with respect to the reference registration is tabulated in table 4. The similarity coefficient is computed as the overlapping volume between a registered CAD model and corresponding reference registration, divided by the total volume of a model. The coefficient varies from 0 (no overlap) to 1 (perfect overlap) (Saiti & Theoharis, 2020).

Table. 4 Object registration results as similarity coefficient to the corresponding reference registration.

DSC [-]	Cube	Wing	Cyclist
Incorporated markers	0.989	0.992	0.971
Multi-point laser	0.989	0.992	0.949
Single-point laser	0.991	0.989	0.949

All registrations return a high value (approximately 0.95 - 0.99) for the similarity coefficients indicating a correct positioning of the CAD model in the measurement space. While the increased surface coverage on the cube using the single-point laser marking seemingly produces higher local values of marker disparity, the similarity coefficient indicates an overall improved matching. Comparatively, the wing and cyclist models maintain a rather constant value of such coefficient, which can be explained by their surface area more frequently in view by the camera triplets (see

section 4.3). The cyclist model registration scores lowest in terms of similarity coefficients, especially for the single- and multi-point laser marking. This is ascribed to the uneven distribution of the manual laser marking, with a larger density towards the positive y-side of the cyclist.

4.3 Modelling of optical occlusion

The object registrations provide a CAD representation of the models used during the experiment, positioned and oriented within the experimental measurement volume/coordinate system. Since the camera locations and orientations are determined within this coordinate system as well, the optical access of the imaging setup can be determined throughout the measurement volume through the use of ray-casting (Möller & Trumbore, 2005). The number of cameras having optical access to a certain region within the measurement volume is referred to as the camera coverage rank R_C. The R_C over the model surface and at the ground plane is visualized in figure 12 for the three objects. The value of R_C on the registered model surfaces provides insight into the observed differences when using incorporated markers or the single-point laser marking from section 4.2. Especially on the cube, R_C = 2 on one of the side faces and the coverage is increased significantly when groups of two cameras are used for a partitioned setup.

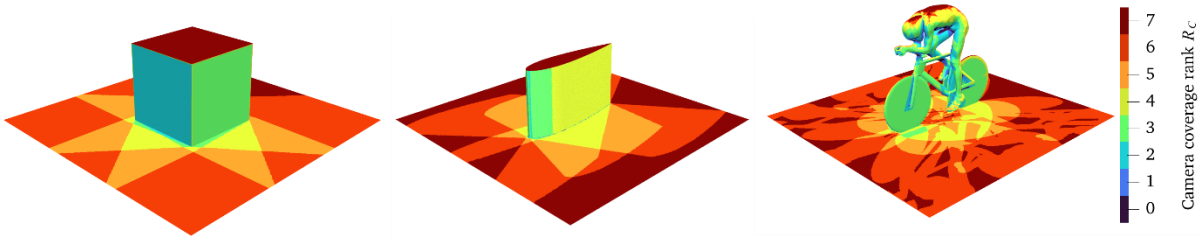

Figure. 12 Camera coverage rank (R_C) of the seven camera imaging setup visualized in a plane at $z = 0\,mm$ for each object.

The variation in the R_C over the planes visualized in figure 12 follows the expected behaviour of the seven camera imaging system as shown in figure 7: out of the three objects, the wing is smallest in height hence there is an R_C of 7 towards the edges of the plane. For all objects, the R_C in the shown planes varies across shapes resembling projected shadows from the perspectives of the individual cameras. For the cube, the majority of the plane at $z = 0\,mm$ features $R_C \geq 3$ with only a small region in front of the frontal face at $R_C = 2$. For the wing and cyclist, the entirety of the plane at $z = 0\,mm$ is in view by at least 3 cameras. The distribution of the R_C throughout the measurement volume is an important factor during the 3D triangulation of flow tracers in particle tracking velocimetry measurements. The volume fraction of the total measurement volume in view by a certain number of cameras is shown in figure 13.

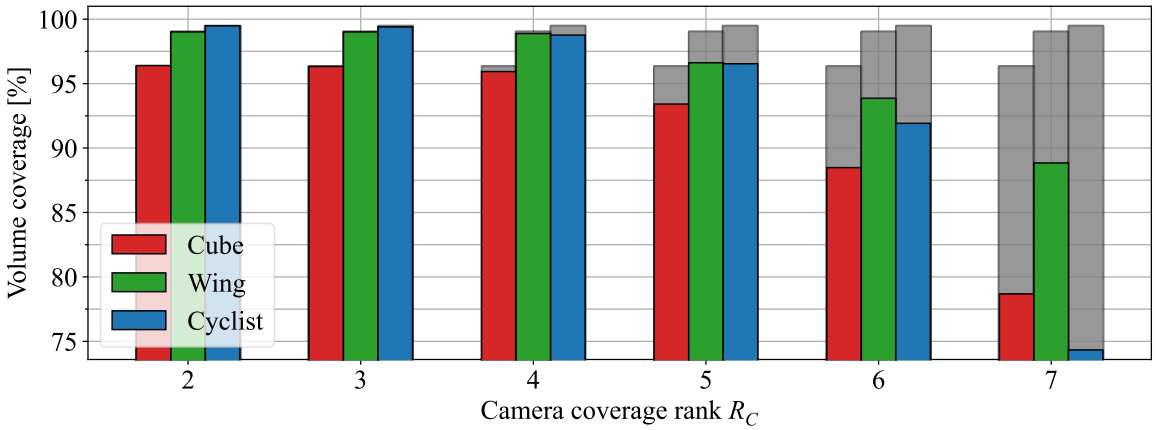

Figure. 13 Measurement volume, effective measurement volume (measurement volume – object volume) and effective measurement volume in view by a certain number of cameras simultaneously (camera coverage rank R_C) for the cube, truncated wing and scaled cyclist object.

The minimum value considered for camera rank is two as it corresponds to the theoretical minimum for 3D determination of a particle position by triangulation. The total volume of the measurement domain (100%) is calculated assuming a cuboid domain of dimensions $0.4\,m \times 0.4\,m \times 0.3\,m$, thus $0.048\,m^3$, centered around the object (as in figure 7). The volume occupied by the object itself is excluded from the calculation. The volumetric coverage decreases by increasing the camera rank, which justifies the frequent adoption of camera system partitioning in 3D experiments. Increasing R_C up to a value of 4 yields minor variations of the volumetric coverage. This behaviour also depends upon the placement of the cameras (as discussed in Hysa et al. 2023) and the shape and orientation of the obstructing object. For instance, the wing, with its smallest height and relatively small thickness, results in the smallest decrease in volume coverage when increasing R_C. Further increasing R_C beyond 5 results in a rapid reduction of volumetric coverage, with the monolithic system yielding a volumetric coverage of below 80% for the cube and cyclist.

The above discussion becomes of vital importance during particle tracking, in the context of the information provided in section 3.4. Without registration of the object in the experimental measurement domain and determination of the variation of the camera coverage rank throughout said domain, a monolithic imaging system is limited in particle triangulations to only the intersected volume of all camera field of views, hence in this experiment the volume coverage at R_C = 7. Additionally, the 'eroded' measurement volume in such a monolithic setup is mostly confined to regions in close proximity of the object surfaces which are especially relevant in the understanding of near wake/surface flow properties. Overcoming such measurement volume erosion can be achieved through partitioning of the imaging setup into independent camera groups as done in section 3.3.1. In a partitioned approach, the measurement volume instead is the union of all regions measured by the camera groups. The downside of the partitioned approach being that a limited number of cameras is used for the triangulation of flow tracers, becoming critical at higher imaging density of seeding particles as typically done in tomographic or particle tracking experiments. The latter circumstance causes the frequent occurrence of ghost particles (Elsinga et al., 2011).

Following the recent work from Wieneke & Rockstroh, (2024) a monolithic approach can be combined with the measurement around an obstructing object if knowledge of the optical

obstructions is introduced. Such an approach is referred to as object aware (OA) monolithic 3D particle imaging. Following the OA-monolithic method, the specific lines-of-sight obstructed by the object are not considered for each camera and particle triangulation can be performed using the optimum (maximum) number of cameras all throughout the domain. This method therefore renders partitioning obsolete and greatly reduces the problem of ghost particles formation.

4.4 Volumetric detection of flow tracers

The volumetric distribution of the camera coverage rank after object registration, such as shown in figure 12, is used to perform OA-particle triangulation/tracking by a monolithic approach. In particular, the iterative particle reconstruction (IPR, Wieneke, 2013) method is used. Three methods of reconstruction are then compared, for the given set of seven cameras: the monolithic approach (M_7-IPR), the partitioned approach with camera triplets (P_3-IPR) and the object aware monolithic method (OA_7-IPR). In figure 14, particle triangulations over 200 measurement snapshots are shown in a $50\ mm$ thick volume set across the freestream directions centered around the midpoint of the object.

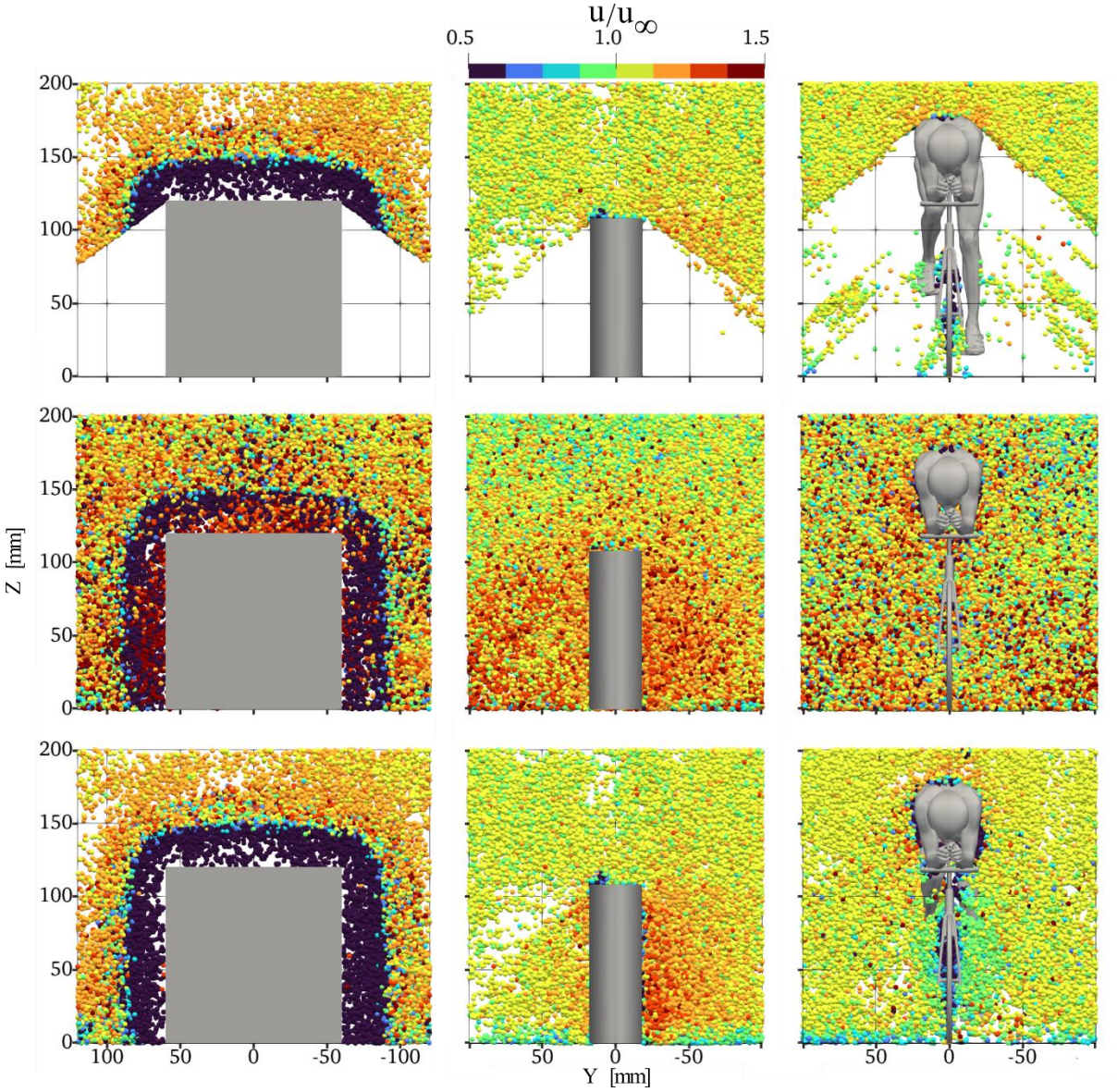

Figure. 14 Particle triangulations in a 50 mm deep $Y-Z$ plane centered at the midpoint of the object. Top row: triangulations using monolithic approach (M_7-IPR). Middle row: triangulations using a partitioned approach (groups of 3, P3-IPR). Bottom row triangulations using object aware monolithic approach (OA_7-IPR). Particles colored by streamwise velocity component.

The top row shows the particles reconstructed using M_7-IPR, where the measurement suffers from significant regions void of particles. These examples illustrate the entity of measurement volume erosion associated to the monolithic approach, as the loss of optical access from each single camera produces a void. In the second row, the reconstruction from P_3-IPR is shown. Clearly, the volumetric coverage is restored, with no clear presence of void regions. The individual particles are color-coded by velocity magnitude. The flow in the region well above the object is expected to exhibit a rather stationary behaviour as it pertains to a potential flow. Instead, in the second row, the scattered occurrence of data with strong variations of the velocity magnitude is associated to erroneous measurements due to ghost particles. Their occurrence is particularly pronounced for P_3-IPR, compared to the monolithic method. The small number of cameras in each sub-group is responsible for this condition (Elsinga et al. 2011).

Furthermore a partitioned setup produces multiple detections of the same tracers in regions where the measurement regions from different camera triplets overlap and data post-processing is required to avoid biasing effects. Ghost particles formed from different camera groups instead, do not coincide and they accumulate in the measurement domain. The analysis performed with OA_7-IPR is shown on the bottom row. The results clearly indicate that both problems of measurement volume erosion and excessive ghost particle formation are mitigated. Particle detection can be performed throughout the measurement volume when in view by at least three cameras, yielding the same volume coverage as the partitioned setup, whilst using more cameras for the triangulation if possible. Not only does this reduce the formation of ghost particles with respect to the partitioned setup but even compared to the monolithic approach. This is especially visible around the cyclist model where in the top figure still a considerable number of unphysical data points are found for M_7-IPR regardless of the involvement of all seven cameras in the triangulation. The reason for this is the large number of particles in the camera images originating from regions in the measurement volume at a R_C of less than seven. Such particles are not triangulated and therefore not eliminated from the particle images leaving them able to contribute to the formation of ghost particles (Schanz et al., 2016; Wieneke, 2013).

4.5 Particle tracking

The ultimate purpose of the experiment is that of obtaining the accurate velocity field distribution around the object of interest. The motion of the detected flow tracers is determined by tracking them throughout the measurement volume. The Shake-The-Box algorithm (STB, Schanz et al., 2016) efficiently performs this task. The number of simultaneously detected tracks over time provides insight into the behaviour of object aware particle tracking (OA_7-STB) compared to the monolithic (M_7-STB) and partitioned STB approach (P_3-STB), this is plotted below in figure 15. Tracks are accepted when a tracer is detected along at least four consecutive timesteps.

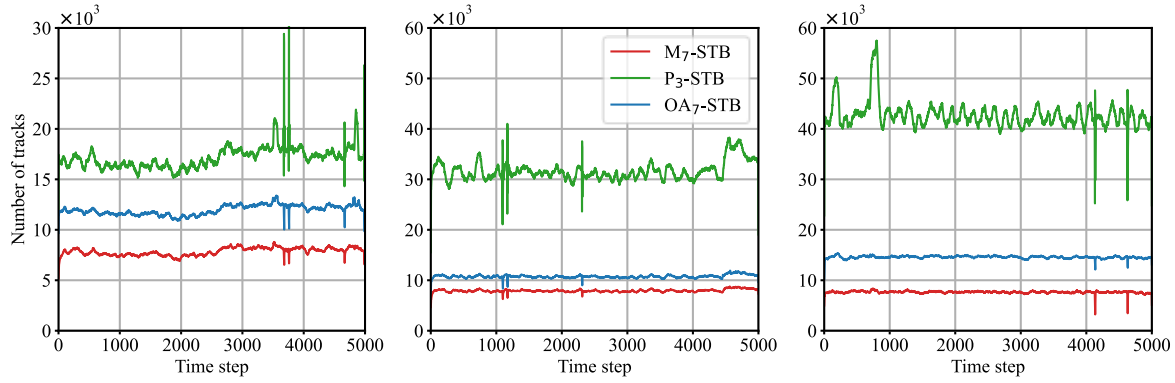

Figure. 15 Number of simultaneously tracked particles using a monolithic (M_7-STB), partitioned (P_3-STB) or OA-monolithic approach (OA_7-STB). Left: cube; middle: truncated wing; right: scaled cyclist.

The monolithic approach yields the smallest number of tracks as a result of the low volumetric coverage. Providing object information restores the measurement volume, with a relative increase in the number of tracks that varies from 40% to 90% depending on the object. The partitioned system produces the largest number of tracks, varying from 2 to 4 times more than the monolithic method. As discussed for the case of the triangulation analysis, such a large number of tracks is

ascribed to the frequent occurrence of ghost particles, which needs to be scrutinized looking at their time coherence. A parameter to consider when assessing the reliability of tracked particles is the tracking ratio, defined as the number of tracked particles (figure 15), divided by the number of triangulated particles. The values of the average tracking ratio are tabulated in table 5.

Table. 5 Average ratio of tracked over triangulated particles (tracking ratio) for the three tracking approaches and objects.

Tracking ratio	Cube	Wing	Cyclist
M_7-STB	0.92	0.87	0.78
P_3-STB	0.2	0.28	0.3
OA_7-STB	0.77	0.74	0.76

Table. 6 Average track length for the three tracking approaches and objects.

Average track length [time steps]	Cube	Wing	Cyclist
M_7-STB	75	54	13
P_3-STB	37	14	17
OA_7-STB	75	50	71

Since ghost particles do not necessarily follow flow trajectories over time, a large number of ghost particles versus true particles results in a low tracking ratio. For the partitioned approach, three to four times lower tracking ratios are observed compared to the monolithic and object aware approaches. This not only indicates a large number of initial ghost particles as was already shown in figure 14, but also results in significantly increased computation times. The monolithic approach makes use of seven cameras for all triangulations and fewer ghost particles are formed with a high tracking ratio as a result. The object aware approach additionally triangulates particles in the regions left void in the monolithic method with as few as three cameras. In such regions, a comparatively larger number of ghost particles occurs, lowering the tracking ratio.

Another parameter of interest is the extent for which a single particle can be tracked throughout time, which is shown in table 6, in terms of average track lengths in timesteps. It should be noted that even though particle triangulations using a simple monolithic approach are limited to regions in view by all seven cameras, once a track has been established, the advancement of the particle only requires that a minimum of three cameras view the particle. This is a specific feature of the STB algorithm, as discussed in Wieneke & Rockstroh (2024) and for other algorithms different logics may be applied to particle detection and tracking. Regions in view by all cameras are typically located away from the objects towards the edges of the measurement volume. Since in these regions particles can be triangulated using the monolithic approach without “object awareness”, particle tracks tend to be initialized far upstream and persist through partially occluded regions resulting in relatively long particle tracks as seen in table 6. The cyclist appears to be an exception to this where many intermittent tracks are observed when crossing interfaces of varying camera coverage R_C resulting in instead much shorter tracks on average. Ghost particles which are assigned to a track typically cannot maintain such a track for extended time resulting in many short tracks instead. This clearly causes a reduced averaged track length for the partitioned setup. The object aware approach can both initialize and track particles all throughout the measurement volume producing similar average track lengths to the non-object aware approach.

Figure 16 reports the diagrams of the number of particle tracks versus their length (time steps). The results pertain to the full sequence of 5000 timesteps. The combined effect on track length and total number of tracks for the different approaches is a clear indicator of method performance and reliability.

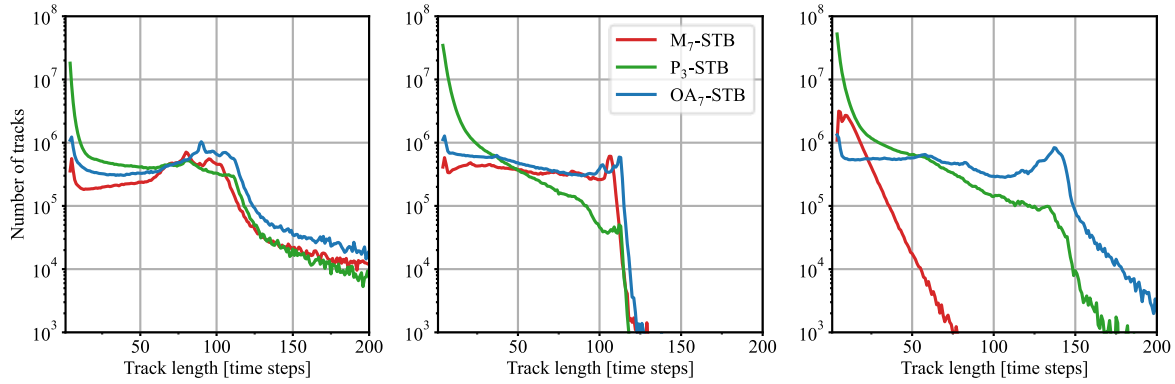

Figure. 16 Track length histogram for three particle tracking approaches. Left: cube; middle: wing; right: cyclist.

The y-axis is shown on a logarithmic scale, given the order of magnitude difference between the occurrence of short tracks (~10 timesteps) for the partitioned system. In line with the expected behaviour of ghost particles, the number of tracks for increasing track length initially drops rapidly. A peak at short track length is also present for the monolithic and object aware methods, however of much smaller magnitude. The value rapidly decreases towards a plateau that lasts till approximately 100 timesteps and then the value decays. This behaviour is expected on the basis of the measurement domain streamwise length, the flow velocity and the chosen sampling frequency. A particle in the freestream at 10 m/s will remain in the domain (of 40 cm length) for approximately 40 ms. At the measurement rate of 3000 fps tracks in the freestream will therefore not exceed 120 timesteps, which justifies the decay on the right end side of the diagrams.
Considering the steep gradient in the partitioned curves until track lengths of roughly 25, tracks with length below 25 seem to contain most of the ghost particles. Filtering out these assumed ghost tracks produces a total number of tracks measured as tabulated below.

Table. 7 Total number of found particle tracks with length bigger or equal to 25 timesteps

Total tracks >= 25 time steps ($\times 10^6$)	Cube	Wing	Cyclist
M_7-STB	34.1	30.8	3.4
P_3-STB	39.2	25.2	44.0
OA_7-STB	49.0	38.8	59.7

Overall, figure 16 and table 7, confirm that the object aware approach yields both a larger number of tracked particles which are tracked over longer periods of time with respect to the simple monolithic approach. Additionally, the formation of ghost particles is noticeably reduced with respect to the partitioned approach.

4.6 Velocity field measurement

The impact of the object registration technique and of the object aware particle reconstruction/tracking is ultimately evaluated in terms of the measured velocity field. The time average velocity distribution is rendered onto a Cartesian grid following the ensemble averaging procedure as described in Agüera et al. (2016). For this, a bin size of $10 \times 10 \times 10\, mm^3$ is used with an overlap percentage of 75%, resulting in a grid spacing of $2.5\, mm$. Within each bin, the velocity is represented by a 2nd order polynomial regression. The streamwise velocity field around

the cyclist is inspected along an $x - z$ plane at $y = 0\ mm$ for the monolithic, partitioned and object aware approaches (figure 17). No filtering is applied to remove measurement noise or to exclude ghost particles from the ensemble at each bin. The freestream velocity for the cyclist was set to $8\ m/s$.

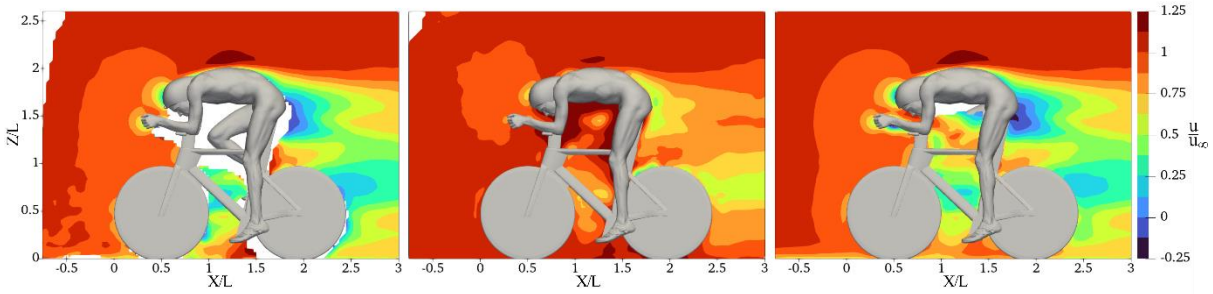

Figure. 17 Normalized streamwise velocity field around the cyclist object. Monolithic (M_7-STB), partitioned (P_3-STB) and OA-monolithic (OA_7-STB) particle tracking approach left to right respectively. Freestream velocity of $8\ \mathrm{m/s}$. Distances normalized by cyclist torso length $\mathrm{L} = 90\ mm$.

The velocity field obtained with the monolithic approach features smaller regions void of data compared to what was shown in figure 14. This is due to the different number of cameras required to triangulate/reconstruct a particle's 3D position (the totality) and to track it using the STB algorithm (only three cameras). The velocity field exhibits a rather uniform value above and upstream of the cyclist, whereas the momentum deficit in the wake is evident, where small regions of reverse flow indicate some local separation at the rear of the athlete. These results are in good agreement with those reported by Jux et al. (2018) who used robotic volumetric PIV around a full-scale cyclist in the same posture, at the racing speed of $14\ m/s$. Even though the velocity field obtained using the partitioned camera setup does not contain any gaps, it is clearly affected by an excessive number of ghost particles. Ghost particles persisting into the tracks typically originate from the coherent motion of bubbles in the freestream and therefore have unphysically high velocities with respect to their neighbouring tracks. This produces a bias error towards larger velocities which tends to decrease the observed velocity gradients (Elsinga et al., 2011). This is clearly visible in the middle figure where there is a complete lack of reversed flow throughout the shown plane and relatively large velocity values in regions of expected stagnation such as the helmet and hands.

The velocity field obtained using the object aware approach largely resembles that of the monolithic system, except for a reduction in the size of the regions void of data below and behind the cyclist torso. Furthermore, for the monolithic approach, regions in view by less than all seven cameras rely on convection of upstream tracks to provide data. This reduces the overall number of tracks used in the ensemble averaging procedure compared to the object aware approach, leading to more jagged velocity contours especially visible upstream of the cyclist and close to the floor.

The random noise caused by ghost particles is examined more closely using the spatial distribution of streamwise velocity fluctuations (standard deviation σ_u) as shown in figure 18.

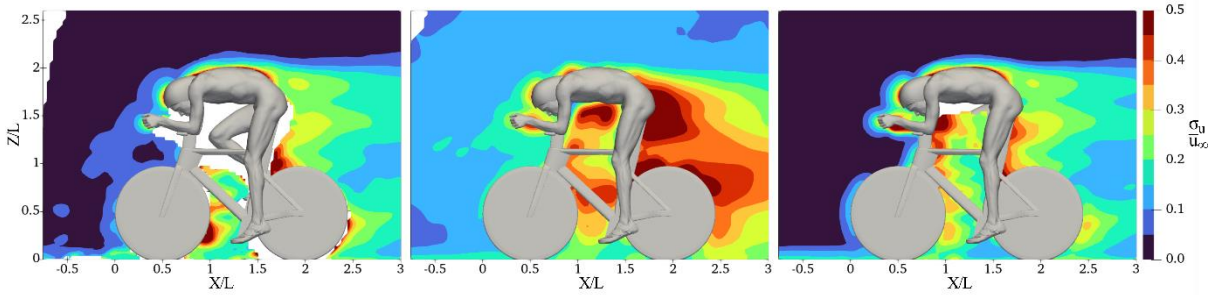

Figure. 18 Normalized standard deviation of the streamwise velocity field around the cyclist object. Monolithic (M_7-STB), partitioned (P_3-STB) and OA-monolithic (OA_7-STB) particle tracking approach left to right respectively. Freestream velocity of 8 m/s. Distances normalized by cyclist torso length $L = 90\ mm$.

The flow regions upstream of the cyclist are expected to exhibit a low level of fluctuations, according to the rated turbulence intensity of the wind tunnel freestream; 0.6% (Pereira et al., 2022). The monolithic approach returns fluctuation levels of approximately 3% and 1.5% when the object aware method is applied. The results from the partitioned setup are considerably corrupted, yielding a standard deviation of up to 12% upstream of the cyclist. A similar pattern is observed in the turbulent wake, where the partitioned method yields fluctuations exceeding 50% of the free-stream value and overall twice as high than those measured with the monolithic approach. It may be concluded that the fluctuating velocity field can only be qualitatively addressed by the partitioned approach, in the present case, where the fluctuations appear to be dominated by the contribution of ghost particles. Especially visible in the object aware approach is an increase in the standard deviation towards regions of flow stagnation. This can be ascribed to unresolved velocity gradients within the relatively large bins used for the ensemble averaging and variations in the bubble response time under acceleration (Faleiros et al., 2019).

5 Conclusion

Object registration methods for volumetric flow measurement techniques are surveyed and compared in the framework of Lagrangian Particle Tracking. Three object marking methods are considered and applied on objects with varying geometrical complexity. Marking the object during manufacturing opens the option to perform object registration using the point-to-point ICP algorithm, offering the highest robustness. The optical marking by a laser pointer or pattern are less invasive and can be applied to a wide variety of objects. Object registration is applied to the objects which are in the order of 10 cm in size and the found discrepancies between registered objects and the triangulated markers are on average in the order of 0.5 mm. The main source of uncertainty is the manufacturing process by 3D printing, followed by the marker size and their amount and distribution over the object surface. The registration accuracy based on the metrics of the similarity coefficients with respect to a reference yields results ranging from 95% to 99%, which is considered sufficiently accurate for the purpose of applying object aware particle reconstruction. Three different regimes of 3D imaging have been considered: monolithic, partitioned and object aware (OA) monolithic. These methods were compared in terms of volumetric coverage of the domain and the ratio between correct tracks and those due to ghost particles. Several benefits of object aware particle tracking are demonstrated. Firstly, the severe problem of erosion of the measurement volume typical of the monolithic multi-camera imaging system is solved, thanks to the selective utilization of cameras with unobstructed views. The second problem noticed for the

partitioned system is the large amount of ghost particles and associated measurement error. Also in this case, the object aware monolithic technique maximizes the number of cameras involved in particle triangulation; dramatically reducing the occurrence of ghost particles, benefitting accurate flow field determination. It may be concluded that partitioning a multi-camera 3D imaging system is the last resort for the measurement around an object and this technique may be considered only when a model for the object is not available or it cannot be reliably measured. Using either statically triangulated incorporated or optical markers, the current approach of object aware particle tracking is limited to rigid and stationary objects with or without a-priori applied markers. In the future, the extension to moving and flexible objects is in principle supported by the framework of object aware particle tracking but will require more sophisticated methods of representing not only the potentially varying position but also shape of the object as a rigid CAD model registration will no longer suffice.

References

Adhikari, D., & Longmire, E. K. (2012). Visual hull method for tomographic PIV measurement of flow around moving objects. Experiments in Fluids, 53(4), 943–964.

Adhikari, D., & Longmire, E. K. (2013). Infrared tomographic PIV and 3D motion tracking system applied to aquatic predator-prey interaction. Measurement Science and Technology, 24(2).

Agüera, N., Cafiero, G., Astarita, T., & Discetti, S. (2016). Ensemble 3D PTV for high resolution turbulent statistics. Measurement Science and Technology, 27(12).

Besl, P. J., & McKay, N. D. (1992). Method for registration of 3-D shapes. Sensor fusion IV: control paradigms and data structures (Vol. 1611, pp. 586-606). Spie.

Bosbach, J., Kühn, M., & Wagner, C. (2009). Large scale particle image velocimetry with helium filled soap bubbles. Experiments in Fluids, 46(3), 539–547.

Cakir, B. O., Gonzalez Saiz, G., Sciacchitano, A., & van Oudheusden, B. (2022). Dense interpolations of LPT data in the presence of generic solid objects. Measurement Science and Technology, 33(12).

Chen, Y., & Medioni, G. (1992). Object modelling by registration of multiple range images. Image and vision computing, 10(3), 145-155.

Depardon, S., Lasserre, J. J., Boueilh, J. C., Brizzi, L. E., & Borée, J. (2005). Skin friction pattern analysis using near-wall PIV. Experiments in Fluids, 39(5), 805–818.

Dice, L. R. (1945). Measures of the Amount of Ecologic Association Between Species (Vol. 26, Issue 3).

Elsinga, G. E., Scarano, F., Wieneke, B., & Van Oudheusden, B. W. (2006). Tomographic particle image velocimetry. Experiments in Fluids, 41(6), 933–947.

Elsinga, G. E., Westerweel, J., Scarano, F., & Novara, M. (2011). On the velocity of ghost particles and the bias errors in Tomographic-PIV. Experiments in Fluids, 50(4), 825–838.

Faleiros, D. E., Tuinstra, M., Sciacchitano, A., & Scarano, F. (2019). Generation and control of helium-filled soap bubbles for PIV. Experiments in Fluids, 60(3).

Grille Guerra, A., Scarano, F., & Sciacchitano, A. (2024). On the scalability of helium-filled soap bubbles for volumetric PIV. Experiments in Fluids, 65(2).

Hysa, I., Tuinstra, M., Sciacchitano, A., & Scarano, F. (2023). A multi-directional redundant 3D-PIV system for ship deck wind interactions. 15th international symposium on particle image velocimetry, San Diego, CA.

Jeon, Y. J., & Sung, H. J. (2012). Three-dimensional PIV measurement of flow around an arbitrarily moving body. Experiments in fluids, 53, 1057-1071.

Jux, C., Sciacchitano, A., & Scarano, F. (2021). Object surface reconstruction from flow tracers. Experiments in Fluids, 62(2).

Jux, C., Sciacchitano, A., Schneiders, J. F. G., & Scarano, F. (2018). Robotic volumetric PIV of a full-scale cyclist. Experiments in Fluids, 59(4).

Langley, K. R., Hardester, E., Thomson, S. L., & Truscott, T. T. (2014). Three-dimensional flow measurements on flapping wings using synthetic aperture PIV. Experiments in Fluids, 55(10).

Lima Pereira, L. T., Ragni, D., Avallone, F., & Scarano, F. (2022). Aeroacoustics of sawtooth trailing-edge serrations under aerodynamic loading. Journal of Sound and Vibration, 537.

Liu, T., Burner, A. W., Jones, T. W., & Barrows, D. A. (2012). Photogrammetric techniques for aerospace applications. In Progress in Aerospace Sciences (Vol. 54, pp. 1–58). Elsevier Ltd.

Mitrotta, F. M., Sodja, J., & Sciacchitano, A. (2022). On the combined flow and structural measurements via robotic volumetric PTV. Measurement Science and Technology, 33(4).

Mendelson, L., & Techet, A. H. (2018). Multi-camera volumetric PIV for the study of jumping fish. Experiments in Fluids, 59(1).

Mertens, C., Fernández, J. L. C., Sodja, J., Sciacchitano, A., & Van Oudheusden, B. W. (2023). Nonintrusive experimental aeroelastic analysis of a highly flexible wing. AIAA Journal, 61(7), 3062–3077.

Möller, T., & Trumbore, B. (2005). Fast, minimum storage ray/triangle intersection. In ACM SIGGRAPH 2005 Courses (pp. 7-es).

Pan, B. (2018). Digital image correlation for surface deformation measurement: Historical developments, recent advances and future goals. In Measurement Science and Technology (Vol. 29, Issue 8). Institute of Physics Publishing.

Pappa, R. S., Black, J. T., Blandino, J. R., Jones, T. W., Danehy, P. M., & Dorrington, A. A. (2003). Dot-Projection Photogrammetry and Videogrammetry of Gossamer Space Structures. Journal of Spacecraft and Rockets, 40(6), 858–867.

Pomerleau, F., Colas, F., Siegwart, R., & Magnenat, S. (2013). Comparing ICP variants on real-world data sets: Open-source library and experimental protocol. Autonomous Robots, 34(3), 133–148.

Rusinkiewicz, S., & Levoy, M. (2001, May). Efficient variants of the ICP algorithm. In Proceedings third international conference on 3-D digital imaging and modeling (pp. 145-152). IEEE.

Saiti, E., & Theoharis, T. (2020). An application independent review of multimodal 3D registration methods. Computers and Graphics (Pergamon), 91, 153–178.

Saiz, G. G., Sciacchitano, A., & Scarano, F. (2022). On the closure of Collar's triangle by optical diagnostics. Experiments in Fluids, 63(8). https://doi.org/10.1007/s00348-022-03468-9

Schanz, D., Gesemann, S., & Schröder, A. (2016). Shake-The-Box: Lagrangian particle tracking at high particle image densities. Experiments in Fluids, 57(5).

Schröder, A., & Schanz, D. (2022). Annual Review of Fluid Mechanics 3D Lagrangian Particle Tracking in Fluid Mechanics. Annu. Rev. Fluid Mech. 2023, 55, 511–540.

Schröder, A., Schanz, D., Bosbach, J., Novara, M., Geisler, R., Agocs, J., & Kohl, A. (2022). Large-scale volumetric flow studies on transport of aerosol particles using a breathing human model with and without face protections. Physics of Fluids, 34(3).

Segal, A., Haehnel, D., & Thrun, S. (2009, June). Generalized-icp. In Robotics: science and systems (Vol. 2, No. 4, p. 435).

Thomas, L., Tremblais, B., Gomit, G., Acher, G., Chatellier, L., & David, L. (n.d.). Simultaneous measurements of flow velocity using Tomo-PIV and deformation of a flexible wing.

Wieneke, B. (2008). Volume self-calibration for 3D particle image velocimetry. Experiments in Fluids, 45(4), 549–556.

Wieneke, B. (2013a). Iterative reconstruction of volumetric particle distribution. Measurement Science and Technology, 24(2).

Wieneke, B., & Rockstroh, T. (2024). Lagrangian particle tracking in the presence of obstructing objects. Measurement Science and Technology.

Zhang, P., Peterson, S. D., & Porfiri, M. (2019). Combined particle image velocimetry/digital image correlation for load estimation. Experimental Thermal and Fluid Science, 100, 207–221.

Zhou, Q.-Y., Park, J., & Koltun, V. (2018). Open3D: A Modern Library for 3D Data Processing.